

Article

# The Evolution of Cast Microstructures on the HAZ Liquefaction Cracking of Mar-M004 Weld

Yi-Hsin Cheng <sup>1</sup>, Jyun-Ting Chen <sup>1</sup>, Ren-Kae Shiue <sup>2</sup>  and Leu-Wen Tsay <sup>1,\*</sup> 

<sup>1</sup> Institute of Materials Engineering, National Taiwan Ocean University, Keelung 202, Taiwan; wk87126@gmail.com (Y.-H.C.); r28051757@yahoo.com.tw (J.-T.C.)

<sup>2</sup> Department of Materials Science and Engineering, National Taiwan University, Taipei 106, Taiwan; rkshiue@ntu.edu.tw

\* Correspondence: b0186@mail.ntou.edu.tw; Tel.: +886-2-2462-2192 (ext. 6405); Fax: +886-2-2462-5324

Received: 31 October 2017; Accepted: 3 January 2018; Published: 5 January 2018

**Abstract:** The causes of liquation cracking in the heat-affected zone (HAZ) of a cast Mar-M004 superalloy weld were investigated. X-ray diffraction (XRD), electron probe microanalyzer (EPMA), and electron backscatter diffraction (EBSD) were applied to identify the final microconstituents at the solidification boundaries of the cast alloy. Fine borides and lamellar eutectics were present in front of some  $\gamma$ - $\gamma'$  colonies, which were expected to be liquefied prematurely during welding. The metal carbide (MC) enriched in Nb, Hf;  $M_3B_2$  and  $M_5B_3$  borides enriched in Cr and Mo; and lamellar Ni-Hf intermetallics were mainly responsible for the induced liquation cracking of the Mar-M004 weld, especially the MC carbides. Scanning electron microscope (SEM) fractographs showed that the fracture features of those liquation cracks were associated with the interdendritic constituents in the cast superalloy.

**Keywords:** liquation crack; heat-affected zone; Mar-M004 superalloy; repair welding

## 1. Introduction

Commercial Ni-based superalloys are widely applied for making critical components in gas turbine engines, which require excellent mechanical and anti-corrosion properties at elevated temperature [1–4]. Mar-M004, a cast Ni-based superalloy, is strengthened primarily by  $Ni_3$  (Al, Ti)  $\gamma'$  precipitates, which are responsible for the stable mechanical properties during long-term applications at elevated temperature [5]. Aeronautic components made of Ni-based superalloys are very expensive and thus costly to maintain or replace during long-term service. To avoid the high expenditure of replacing damaged turbine blades, damaged components can be rejuvenated by fusion welding, which is one of the most accessible processes for commercial maintenance [6].

In general, precipitation-hardened Ni-based superalloys have very poor weldability, especially alloys with high (Al + Ti) contents [6]. Liquidation cracking in the HAZ is one of the most noticeable problems in welding or repair-welding of Ni-based superalloys such as IN 738 [7–9], Rene 80 [10–13], IN 939 [14,15], RR 1000 [16], IN 713C [17], and K465 [18]. Grain boundary liquation results from incipient melting of MC carbides, Cr-Mo borides,  $\gamma$ - $\gamma'$  eutectic and Ni-Zr intermetallics along the solidified boundaries [18–24]. The use of filler metals with (a) slower aging response, (b) smaller lattice mismatch between the precipitates and the matrix, (c) lowered (Ti + Al) concentrations and (d) softer weld metal have been reported to reduce the HAZ cracking susceptibility of IN 738LC welds [25]. Moreover, preweld heat treatments [10,14,15,22–24] have been conducted to modify the microstructures of precipitate-strengthened Ni-based superalloys to decrease the sensitivity of liquidation cracking in the HAZ.

In this work, a cast Mar-M004 superalloy was welded by tungsten-inert gas arc welding process. The effects of inherent microconstituents at the solidified boundaries of cast Mar-M004 superalloy on the HAZ liquation cracking were investigated. The microstructures were examined mainly by a scanning electron microscope (SEM) equipped with an energy-dispersive x-ray (EDX) or electron probe microanalyzer (EPMA) to determine the chemical compositions of those complex constituents along the solidified boundaries. The phase constitutions at the grain boundaries of the specimens were also identified by electron backscatter diffraction (EBSD). The relationship between microstructural features and hot cracking sensitivity of the Mar-M004 superalloy weld was correlated in this study.

## 2. Materials and Experimental Procedures

The Mar-M004 alloy plate used in this study was wire-cut from a cast turbine disc to dimensions of 70 mm × 35 mm × 4.0 mm. The nominal chemical compositions of the experimental material in weight percent were 0.05C, 5.95Al, 0.6Ti, 12Cr, 4.5Mo, 2Nb, 1.3Hf, 0.05Zr, 0.015B, and balance Ni. The as-cast Mar-M004 alloy was further subjected to stress relief treatment at 1050 °C for 5 h in high vacuum ( $<5 \times 10^{-5}$  Pa) before wire-cutting. To simulate the repair-welding of surface and sub-surface defects on the turbine blade, a blind hole with a 90° bevel angle, a depth of 3.2 mm and a tip radius of 1.6 mm was machined on the substrate. A gas tungsten arc welding process coupled with IN 625 rod as the filler was used to arc-melt and fill the blind hole. After welding, the samples were cut either normal or parallel to the top of weld surface. Metallographic preparations were made on the repair welds, with special attention paid to the HAZ microcracks.

The microstructures of the substrate and weld were inspected by field emission scanning electron microscope (FESEM). The chemical compositions of the different phases present at the solidified boundaries were determined by either energy dispersive spectroscopy (EDS) or electron probe microanalyzer (EPMA). Fractographs of the cracked specimens were inspected by using a scanning electron microscope (SEM). To identify the phase constitutions at the grain boundaries, the specimens were examined by an SEM equipped with a NordlysMax<sup>2</sup> electron backscatter diffraction (EBSD) detector.

## 3. Results and Discussion

### 3.1. Microstructural Examinations

Figure 1 displays the microstructures of the cast Mar-M004 alloy. The MC carbides were the primary second phase along the dendrite boundaries (Figure 1a). The results also revealed MC carbides with distinct shapes, including island-like, blocky and Chinese-script. As the solidification proceeded during casting, the segregation of alloy elements caused various solidification microconstituents to form at interdendritic boundaries, as shown in Figure 1b. The results indicated the presence of lamellar eutectic in front of  $\gamma$ - $\gamma'$  eutectic colonies implying the enhanced formation of low melting microconstituents at the solidification boundaries. For the phase contrast inspection by SEM with backscatter electron (BSE), the image brightness was strongly related to the solidification products. Figure 1c,d are BSE images showing different solidification products in front of  $\gamma$ - $\gamma'$  eutectic colonies. Moreover, the EPMA was applied to determine the compositions of those microconstituents at the interdendritic boundaries.

Table 1 lists the chemical compositions (in at %) of the EPMA analysis results, which were measured at different sites indicated in Figure 1c,d. As listed in Table 1, the MC carbides (Figure 1c, site 1) were rich in Nb with additional Hf and Ti. Due to the high Nb and Hf contents, the MC carbides showed high brightness in the BSE image. It was noticed that the MC carbides comprised of 4 at % B; it implied few B atoms dissolved into the MC carbides. The results of EPMA confirmed that the MC carbides could have different morphologies; i.e., either blocky or point-array (Figure 1c, site 2). The relatively low Nb, Hf, and Ti contents at site 2, as compared to those at site 1, could be attributed to the interference of background-alloying. Figure 1d displays complex microconstituents in association

with the  $\gamma$ - $\gamma'$  eutectic colony, including gray blocky product (site 3) and bright lamellar eutectic (site 4). The EPMA results indicated that the gray blocky product had a high boron content and was enriched in Cr and Mo. Furthermore, the bright lamellar eutectic showed co-segregation of Hf and Zr. The low alloy contents of the measurement (site 4) were also attributed to the high yield volume of the electron beam relative to the width of the lamellar structure.

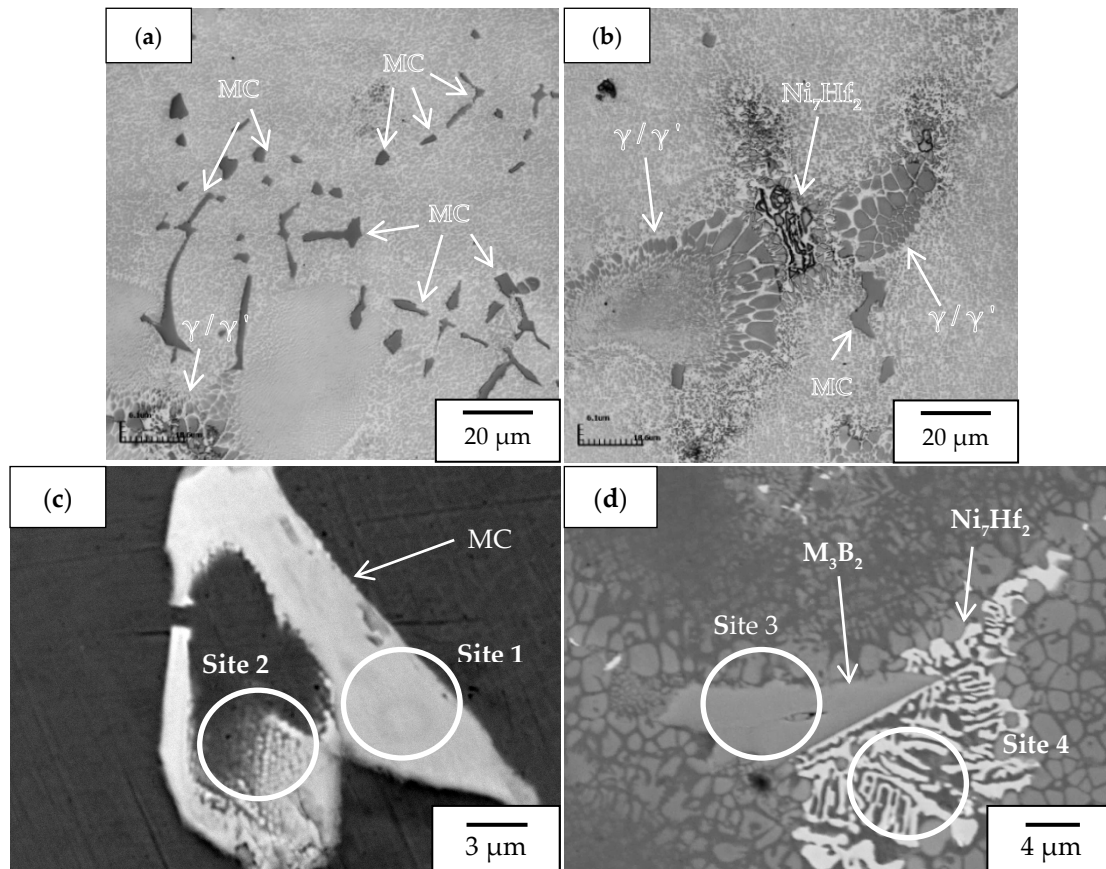


**Figure 1.** Optical micrographs of (a) MC carbides; (b)  $\gamma$ - $\gamma'$  eutectic colonies and other solidification products; BSE images of FESEM displaying (c) enlarged view of MC carbides; (d) lamellar microconstituent along boundaries.

**Table 1.** The chemical compositions in at % of the solidification products indicated in Figure 1.

Element	Cr	Al	Mo	Nb	Hf	Ti	C	Zr	B	Ni
Site 1	0.65	0.06	4.11	31.68	6.51	6.40	43.57	0.36	4.00	Bal.
Site 2	3.05	7.98	2.65	21.32	4.30	4.82	21.11	0.37		Bal.
Site 3	23.82	0.01	29.71	2.26	0.12	0.11	0.57	0.04	39.99	Bal.
Site 4	9.24	3.31	2.20	1.62	6.23	0.70	2.86	3.32		Bal.

Figure 2 presents XRD patterns of the cast Mar-M004 alloy. MC carbides,  $M_5B_3$  and  $M_3B_2$  borides, and  $Ni_7Hf_2$  intermetallics associated with  $\gamma'$  precipitates in the  $\gamma$  matrix were identified. In the prior studies [8,19], complex grain boundary constituents, such as MC carbides,  $M_2SC$  sulphocarbides, Cr-Mo borides, Ni-Zr intermetallic compound and  $\gamma$ - $\gamma'$  ( $Ni_3(Al,Ti)$ ) eutectics were obtained in IN738/IN738LC superalloy. The presence of those terminal solidification products at interdendritic boundaries was inevitably detrimental to the weldability of the cast Mar-M004 superalloy.

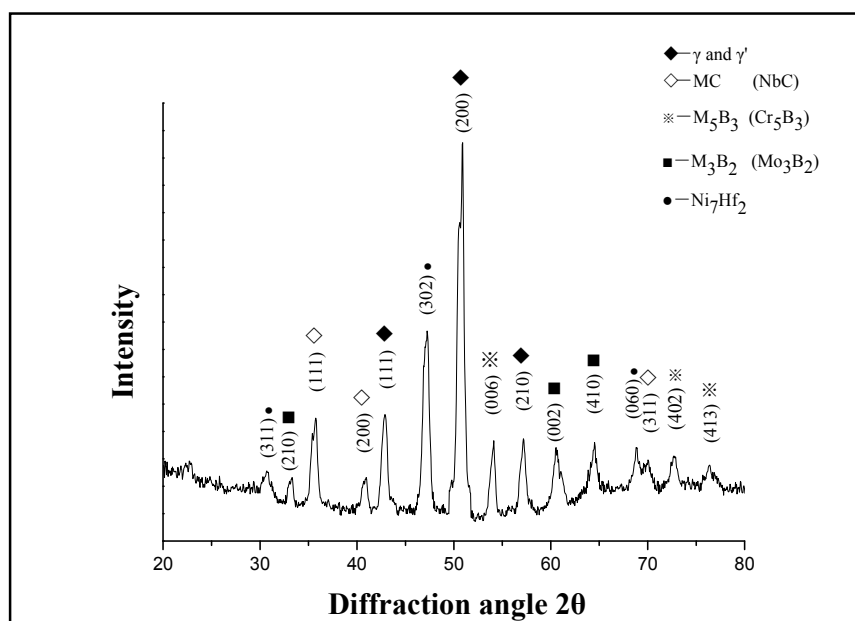
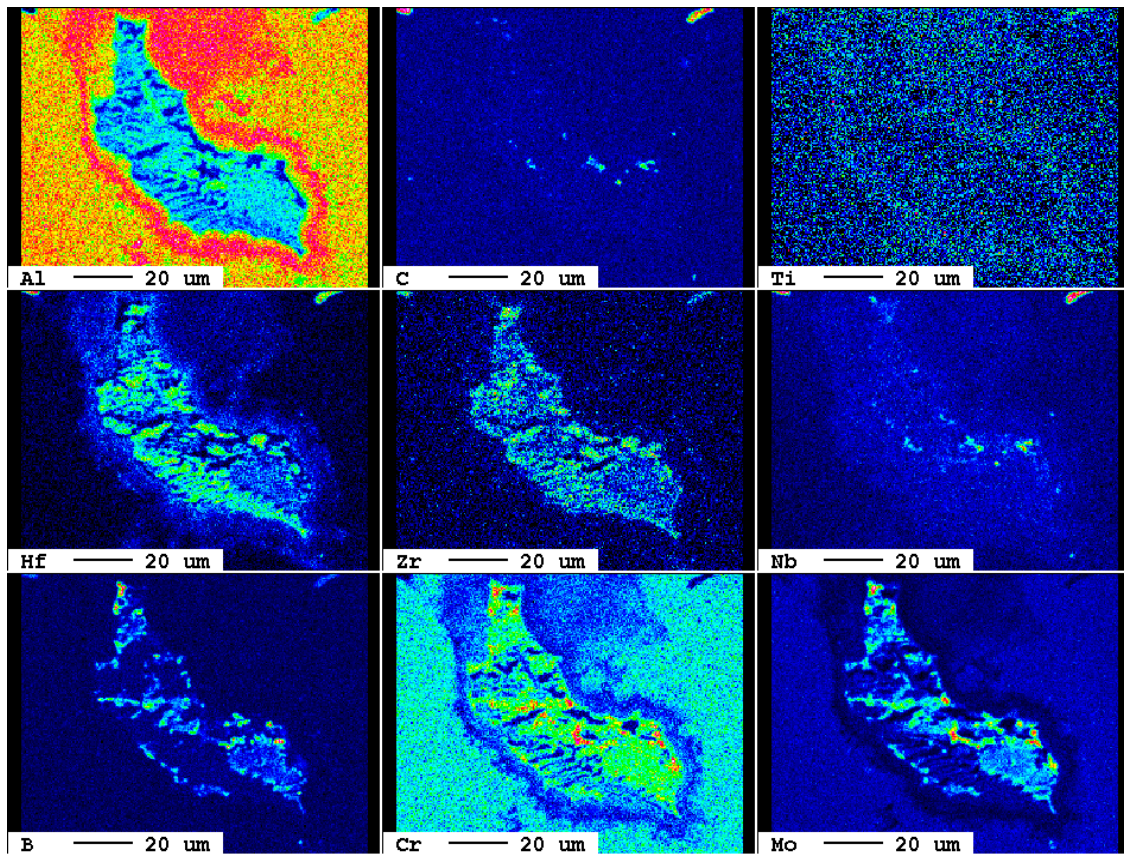
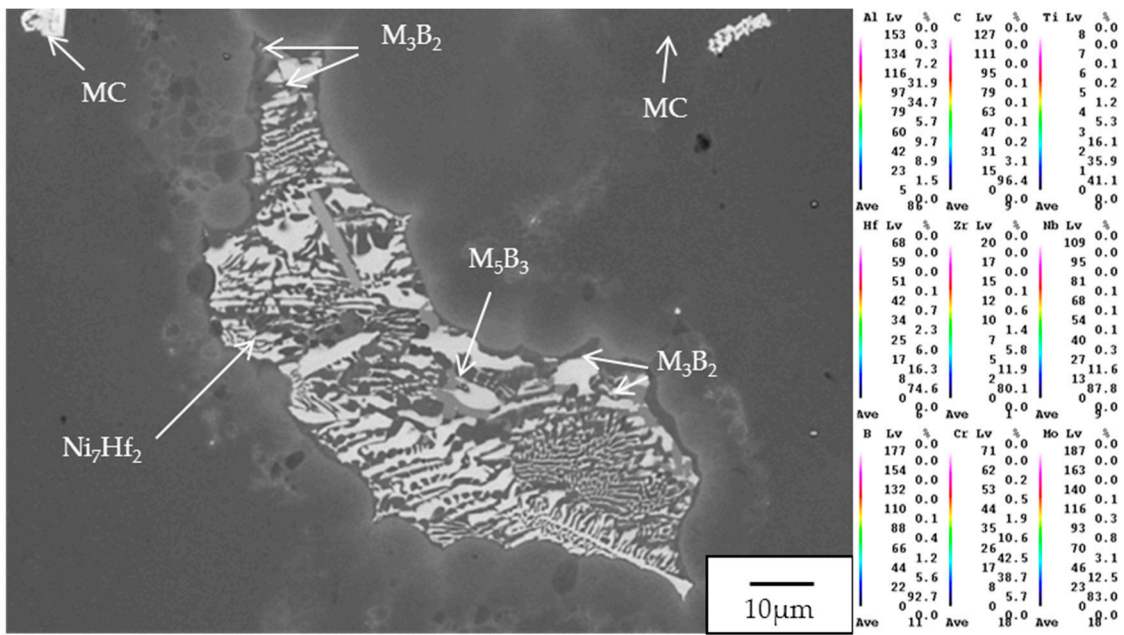


Figure 2. X-ray diffraction patterns of the cast Mar-M004 superalloy.

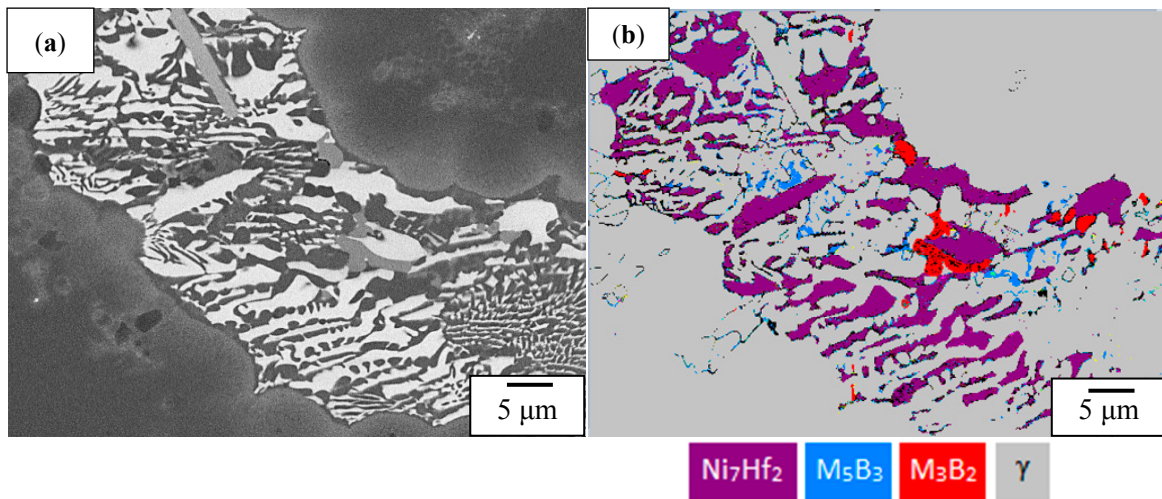
Figure 3 presents the EPMA mappings in order to reveal the distributions of various alloy elements in the interdendritic microconstituents. The color guide in element mapping analysis consists of two columns, i.e., Lv and %. For example in the Al mapping, the column with Lv caption stands for the total count number of Al. A bright color is associated with higher count numbers than that of a dark one. The column with % caption is the area fraction of related color in the Al mapping. For the Al mappings in Figure 3, the area fractions of red and yellow are 31.9% and 34.7%, respectively. Basically, the grain boundary products were lean in Al and rich in Hf, Zr, Cr and Mo. Al element tended to profile the grain boundary microconstituents, in which was associated with the  $\gamma$ - $\gamma'$  colonies. In addition, It seemed that Ti did not segregate severely to the  $\gamma$ - $\gamma'$  colonies. The C combined with the Nb (carbide former) to form MC carbide. In contrast, the B was prone to segregate into the final solidification product. Moreover, the location with high B intensity was also enriched with Cr and Mo elements. Based on the morphology and image brightness of the grain boundary products, (Cr,Mo)-borides in different shapes were inter-dispersed in the final solidification product. The results also indicated that not all Zr and Hf co-segregated with C to form carbides. In fact, lamellar eutectics were rich in Hf and Zr and lean in C, which were response for their high brightness in the micrograph. It was deduced that the formation of Ni-Hf-Zr intermetallics was related to the results, and will be confirmed later in the text.

### 3.2. Phase Identification by EBSD Analysis

Interdendritic microconstituents were examined by FESEM in BSE image and identified by EBSD, as shown in Figure 4. The BSE image (Figure 4a) shows that the solidification product seemed to be composed of several phases in different brightness. The phases identified by EBSD should be consistent with their chemical compositions (Figure 3b) and image contrast (Figure 4a). As shown in Figure 4b, the final solidification products consisted of mainly  $\text{Ni}_7\text{Hf}_2$  intermetallic compound, a few  $\text{M}_3\text{B}_2$  boride particles (red phase) and many fine  $\text{M}_5\text{B}_3$  compounds (blue phase) interspersed in the lamellar eutectics. Based on their compositions displayed in Figure 3, the intermetallic compound was rich in Hf and Zr, but lean in C and B. Obviously, the Ni-Hf intermetallics had very low solubility of the C and B. In contrast, the B could be detected in other zones of the solidification products. The results also indicated that  $\text{M}_3\text{B}_2$  and  $\text{M}_5\text{B}_3$  borides were enriched with Cr and Mo elements. The EBSD results shown in Figure 4b are in accordance with the EPMA analysis shown in Figure 3.



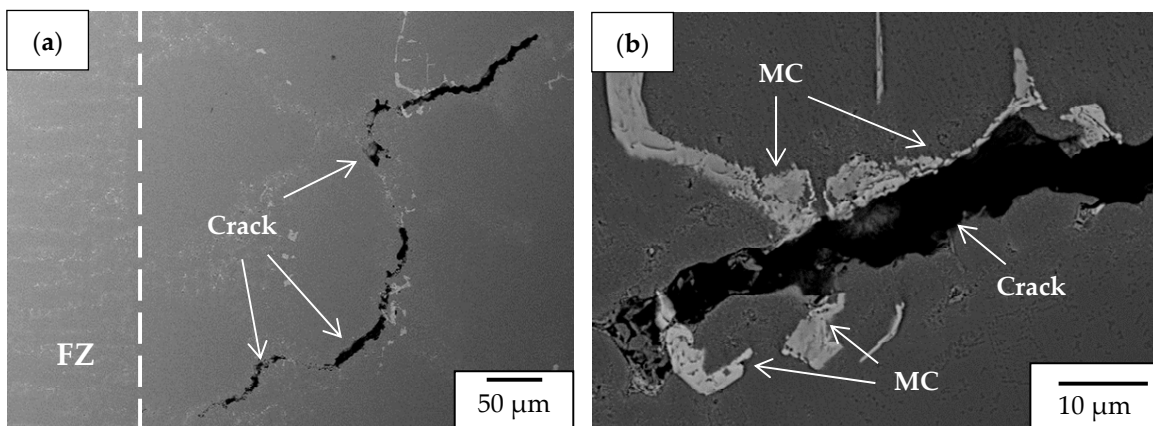
**Figure 3.** BSE image of the interdendritic product and the associated EPMA maps of the Al, C, Ti, Hf, Zr, Nb, B, Cr, Mo elements in the microconstituent.



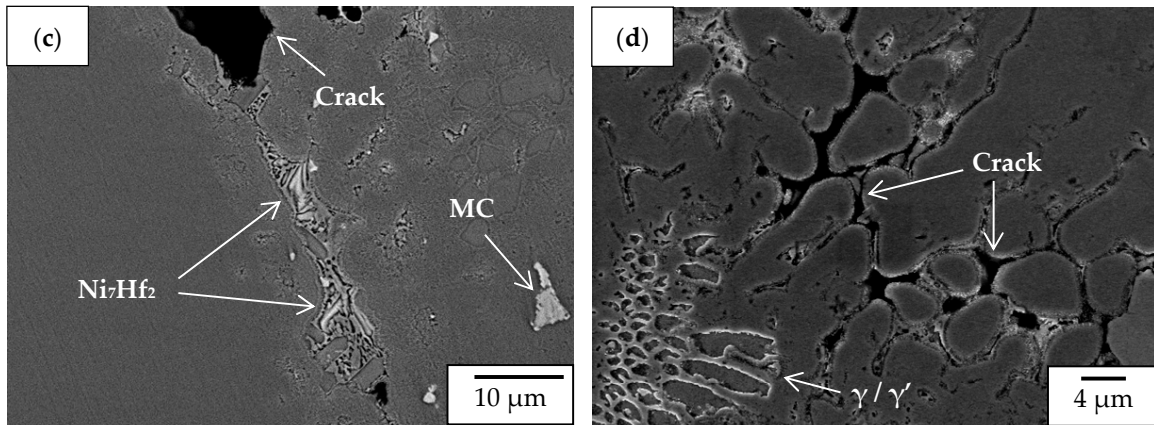
**Figure 4.** (a) BSE image of FESEM of the solidified products; (b) EBSD map to identify distinct phases.

### 3.3. HAZ Microcrack Inspection and Phase Identifications

The welds were prepared by standard metallurgical procedures before inspection. Microcracks were found mainly in the HAZ, but very few in the fusion zone. Figure 5 presents BSE images of FESEM showing the HAZ microcracks adjacent to the fusion zone (FZ) of the tungsten inert gas welds. It was obvious that these microcracks propagated interdendritically in the HAZ of the weld (Figure 5a). The induced microcracks were strongly related to inherent metallurgical factors of the Mar-M004 superalloy. As reported in previous works [20,21,24,25], constitutional liquation of MC carbides,  $M_3B_2$  borides,  $M_2SC$  sulfocarbides,  $\gamma'$  particles, and  $\gamma$ - $\gamma'$  eutectic accounts for the HAZ liquation cracking of IN 738 superalloy weld. The cracks were prone to propagate along the interfaces between the MC carbide and the matrix (Figure 5b), owing to substantial amount of MC carbides in the cast Mar-M004 superalloy. Moreover, microconstituents in lamellar form also contributed to HAZ liquation cracking, shown in Figure 5c. Solidification cracks were also found to initiate and propagate along the interfaces between the  $\gamma$ - $\gamma'$  colonies, which were reported in prior studies [7,10,15,18] (Figure 5d). Constitutional liquation of coarse  $\gamma'$  particles at the boundaries, which do not dissolve into the matrix during heating cycles, contributes to the HAZ liquation cracking [16,21].

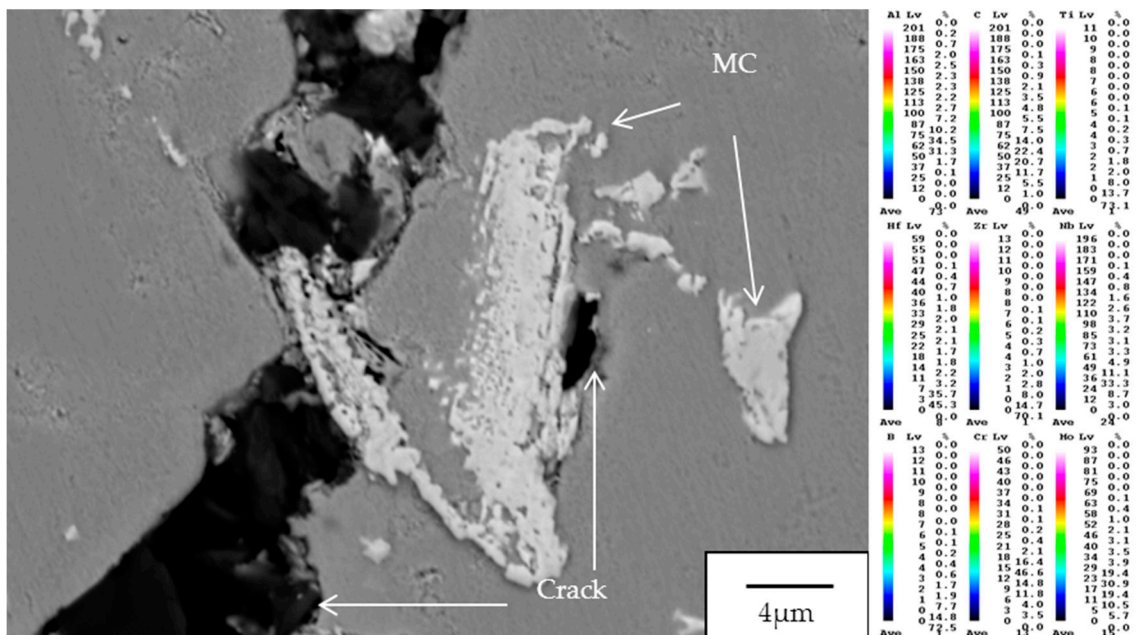


**Figure 5.** Cont.

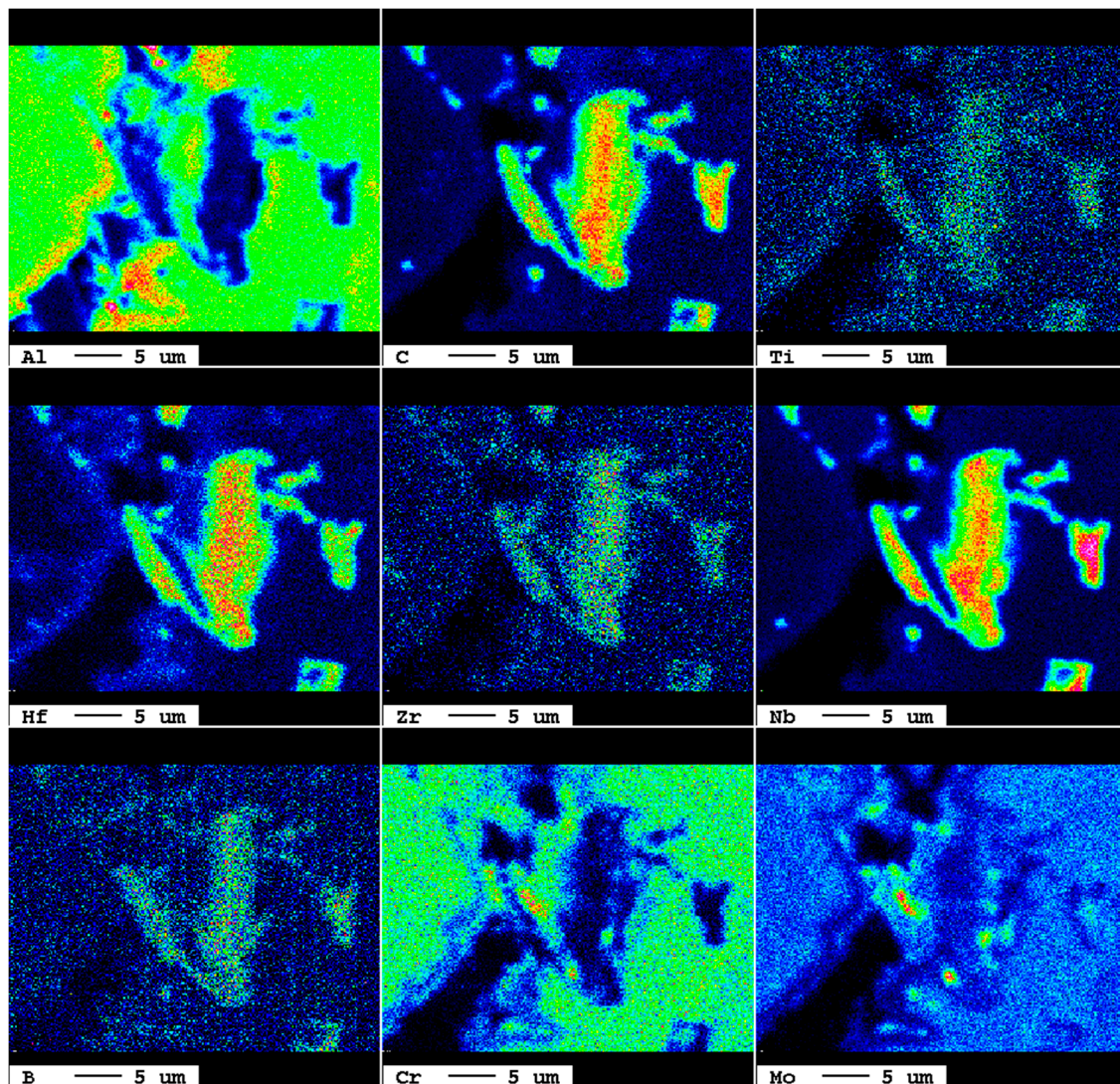


**Figure 5.** (a) Liquation cracks at the HAZ of the Mar-M004 weld; (b) crack propagating along the interface of the MC carbide and matrix; (c) lamellar white phases ahead of liquation crack; (d) solidification cracking along  $\gamma$ - $\gamma'$  colonies.

Regarding the HAZ cracks shown in Figure 5, the causes for the cracking were investigated by determining the compositions and identified those harmful species around the cracks. Figure 6 shows the EPMA element maps of the solidified products associated with the HAZ cracking. A microcrack indicated by the arrow of about 4 μm length was present, which displayed the initiated separation between the carbide and the matrix. The distribution of C and B was used to distinguish the types of microconstituents in the superalloy. The results indicated that the grain boundary product with high brightness was enriched in C, Hf, Nb, Zr, and Ti, but depleted from Al, Cr and Mo. It was deduced that the grain boundary product was MC carbides enriched in distinct carbide formers. In addition, the B and C were found to co-segregate to the MC carbides. Similar results as observed in Table 1 indicated that the MC carbides was alloyed by a certain amount of B. Regarding the distributions of Cr and Mo in Figure 6, the locations of high Cr and Mo contents along with B were prone to form fine Cr-Mo borides embedded in the MC carbides.



**Figure 6.** Cont.



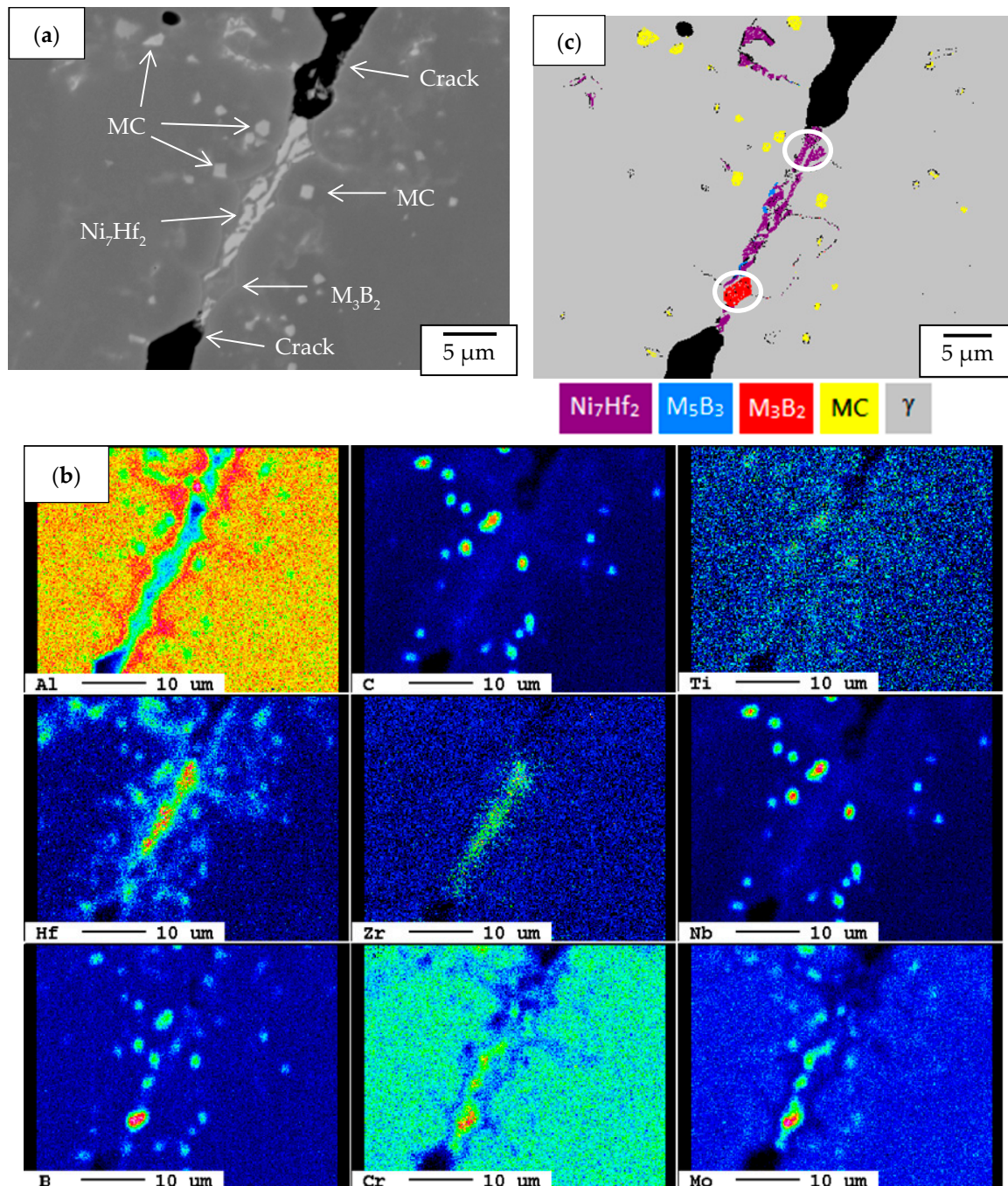
**Figure 6.** BSE image of FESEM of the liquated carbides in the HAZ and EPMA maps of the Al, C, Ti, Hf, Zr, Nb, B, Cr, Mo elements in the MC carbides.

Figure 7 presents the BSE image of FESEM (Figure 7a), EPMA element (Figure 7b) and EBSD maps (Figure 7c) in order to characterize the solidified products ahead of liquation cracks. The EPMA maps (Figure 7b) of the interdendritic microconstituents were linked with the morphologies (Figure 7a) and phase constituents (Figure 7c) in the cast Mar-M004 superalloy. Fine MC carbide particles (Figure 7a), which possessed high Nb and Hf concentrations (Figure 7b), were around the crack path. As shown in Figure 7a, Cr-Mo boride and lamellar eutectics seemed to line up with the interdendritic boundary. EPMA maps showed high concentration of Al profiling the grain boundary white phases, which could be related with the  $\gamma$ - $\gamma'$  colonies or coarse  $\gamma'$  precipitates. Similar to prior analysis, the enrichment in B was found in the MC carbide particles (Figure 7b). The BSE image (Figure 7a) showed the white phase ahead of the crack tip was rich in Hf and Zr (Figure 7b). High Hf and Zr contents in the white phase naturally revealed high brightness in BSE image (Figure 7a). As listed in Table 2, the boride and intermetallic had their own alloy elements. The EBSD map (Figure 7c) revealed that  $M_3B_2$  boride was in the form of blocky particle, the  $Ni_7Hf_2$  intermetallics was more likely in the lamellar form, and slender  $M_5B_3$  borides were interspersed in the  $Ni_7Hf_2$  intermetallic compounds. The results indicated complex solidification species were formed during the final stage of solidification. The existence of low-temperature eutectics formed at the interdendritic boundaries inevitably depressed the terminal

solidification to a much lower temperature, thereby contributing to the HAZ liquation cracking of the cast Mar-M004 weld.

**Table 2.** EPMA chemical compositions in at % of the solidification products ahead of the liquation cracks indicated in Figure 7c.

Element	Cr	Al	Mo	Nb	Hf	Ti	C	Zr	B	Ni
Ni <sub>7</sub> Hf <sub>2</sub>	2.92	1.19	0.64	1.89	12.52	0.90	5.43	2.69		Bal.
M <sub>3</sub> B <sub>2</sub>	31.99	0.04	33.55	2.21	0.04	0.20	1.02		26.95	Bal.



**Figure 7.** (a) BSE image of FESEM showing the microstructures ahead of liquated cracks and (b) the EPMA element maps; (c) EBSD map to identify distinct phases.

### 3.4. SEM Fractographs

Figure 8 displays SEM fractographs in BSE image of HAZ microcracks in a Mar-M004 alloy weld. After cutting and metallurgical preparation of the cracked weld, the HAZ microcracks were opened by a bending fixture after the weld was immersed into the liquid N<sub>2</sub> for a few seconds. The smooth fractured surface displayed solidified liquid droplet features with some terminal solidification products on it (Figure 8a,b). Those grain boundary microconstituents found in the cast superalloy were also observed on the fracture surface of the opened liquation cracks. The coverings on the surface had different morphologies including blocky, array-particles and worm-like. The chemical compositions of those coverings (Figure 8) were determined by using the EPMA, and the results were listed in Table 3. It indicated that the solidification products causing cracking were MC carbides enriched in Nb along with Hf and Ti. Obviously, localized melting of grain boundary microconstituents during welding led to HAZ liquation cracking. According to the carbide features on the fractured surface, it was deduced that the  $\gamma$ /MC eutectics was mainly responsible for the liquation cracking in the HAZ of Mar-M004 weld.

**Table 3.** EPMA chemical compositions in at % of the solidification products indicated in Figure 8.

Element	Cr	Al	Mo	Nb	Hf	Ti	C	Zr	Ni
Site 1	1.36	0.07	1.21	18.43	15.95	3.17	50.82	1.89	Bal.
Site 2	0.61	1.86	4.69	29.39	5.31	7.04	38.63	0.38	Bal.
Site 3	0.28	1.24	1.67	24.27	4.34	4.29	49.65	0.43	Bal.

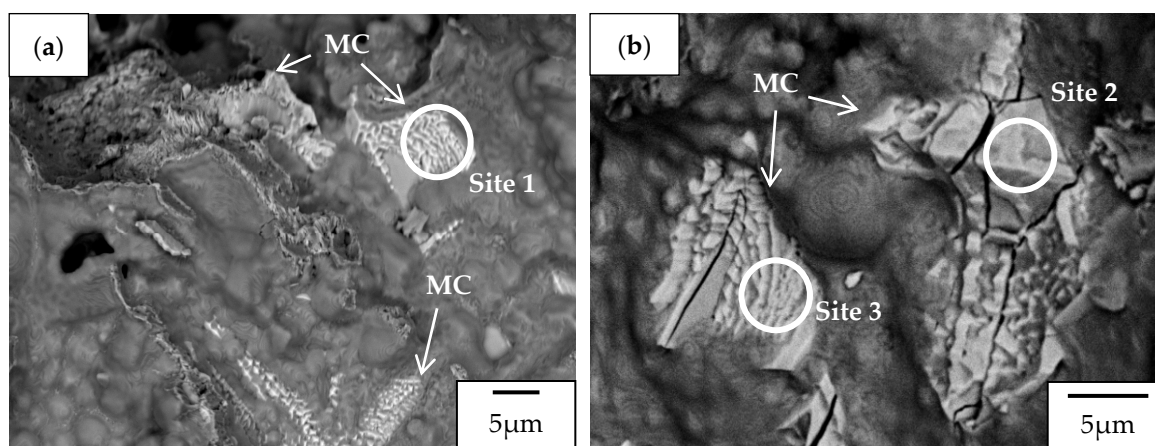


**Figure 8.** SEM fractographs: (a) solidified droplet features covered by final solidification products; (b) eutectic microconstituents associated with liquation cracking.

Figure 9 shows the fracture appearance of the liquation crack and associated EPMA element maps. The fracture surface covered by low melting products was associated with a low Al content, but it was rich in C, Nb, Hf, and Ti. It was deduced that the segregation of strong carbide formers during solidification caused the formation of MC carbides, and assisted the  $\gamma$ /MC eutectic reactions. The depressed solidification temperatures increased the tendency of liquation cracking under the action of weld-shrinkage stress. Consistent with prior analysis by EPMA, the B atoms co-segregated with C to the grain boundaries; therefore, the MC carbides contained a certain amount of B. Moreover, some local sites consisted of very high Cr and Mo concentrations along with high B intensity, suggesting that fine boride particles might be formed at such sites. The presence of borides is reported to facilitate liquation at low temperature and enlarge the brittle temperature range, thus increasing the susceptibility of HAZ liquation cracking [22]. The segregation of B into the grain boundary carbides along with

the formation of  $M_3B_2$  and  $M_5B_3$  borides therein would further deteriorate the weldability of cast Mar-M004 superalloy.

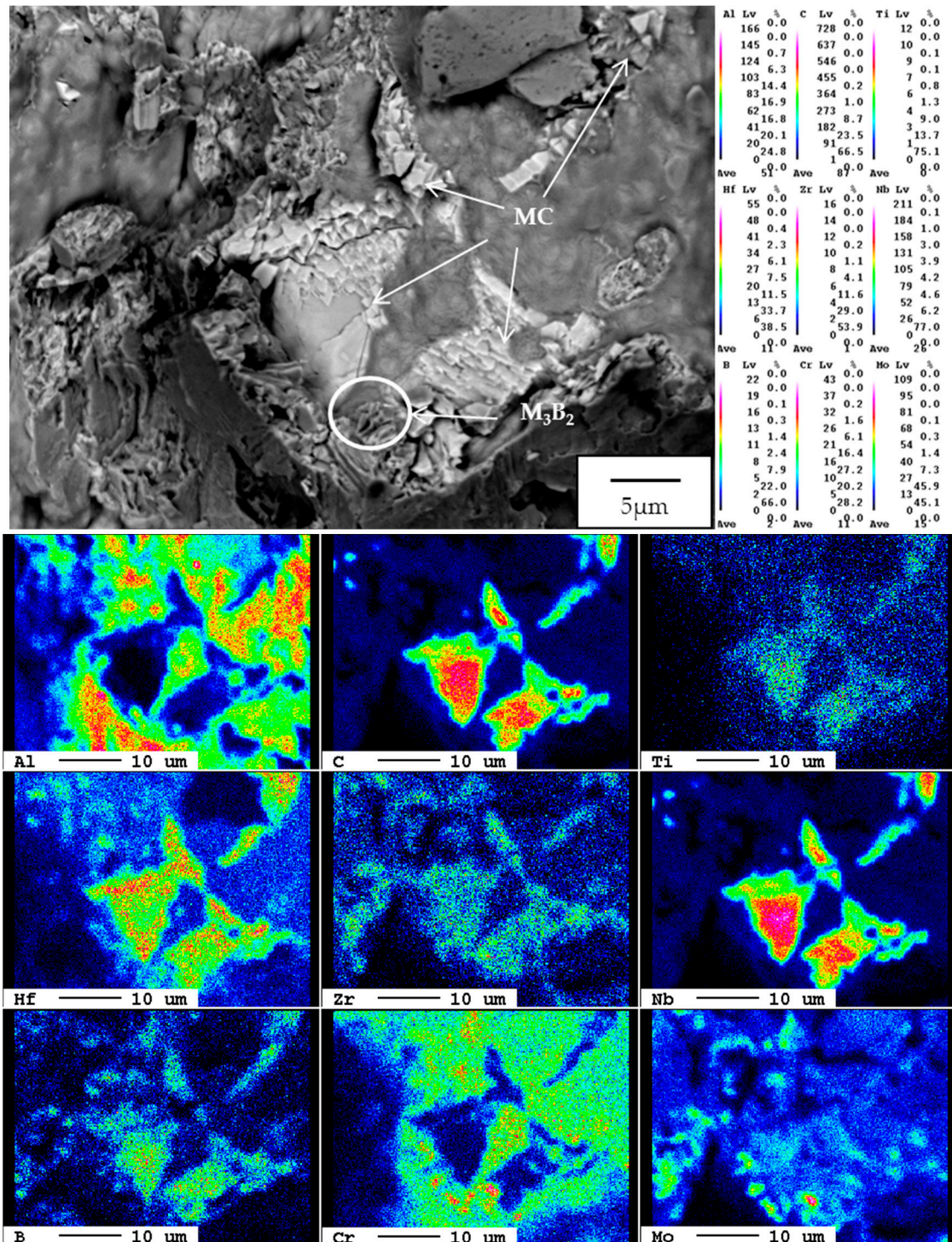


**Figure 9.** SEM fractograph of liquation crack and the associated EPMA maps of the Al, C, Ti, Hf, Zr, Nb, B, Cr, Mo elements on the fracture surface.

The cast Mar-M004 superalloy comprised of complex solidification products at the interdendritic boundaries. The MC carbides were rich in Nb, Hf and Ti alloyed with a certain amount of B. Cr-Mo borides and Ni-Hf intermetallics in lamellar form were found to locate in front of the  $\gamma$ - $\gamma'$

colonies, in which associated with the terminal solidification stage. The high Al content of the Mar-M004 superalloy assisted the strong segregation of this element to the boundaries of the  $\gamma$ - $\gamma'$  colonies, which might lower the melting temperature therein. The results indicated that the HAZ microcracks in the cast Mar-M004 weld initiated and propagated mainly along the  $\gamma$ /MC interface, and/or the boundaries of the  $\gamma$ - $\gamma'$  colonies. The presence of those low-melting constituents at the solidification boundaries of the cast Mar-M004 was responsible for liquation-cracking of the weld. Therefore, the weldability of the cast Mar-M004 superalloy could be improved by reducing or eliminating those harmful microconstituents. To remove the borides and intermetallics at the boundaries, pre-weld heat treatment of the superalloy will be conducted in the future work.

#### 4. Conclusions

Liquation cracking in the heat-affected zone (HAZ) of a cast Mar-M004 weld was investigated in this study. The cast Mar-M004 superalloy consisted of extensive precipitation of ordered  $\gamma'$  intermetallics in the matrix along with various microconstituents at interdendritic boundaries. The occurrence of liquation cracking in the HAZ of the Mar-M004 weld was associated with the eutectic melting of final solidification products at the grain boundaries, such as MC carbides, Cr-Mo borides and Ni-Hf intermetallic compounds, especially the MC carbides. Moreover, it was noticed that the co-segregation of B with C enhanced the formation of MC carbides alloyed with a certain amount of B. It was deduced that residual liquid with high B content enhanced the formation of borides and M(CB) carbides at the interdendritic boundaries, resulting in further deteriorating weldability of the cast Mar-M004 superalloy.

**Acknowledgments:** The authors gratefully acknowledge the financial support of this investigation by the Ministry of Science and Technology, ROC (Contract No. MOST 104-2221-E-019-003). The authors also appreciate Chung-Yuan Kao for his great help in EPMA analyses at National Taiwan University.

**Author Contributions:** Leu-Wen Tsay and Ren-Kae Shiue designed and planned the experiment. Yi-Hsin Cheng and Jyun-Ting Chen performed the experiment. All co-authors contributed to the manuscript proof and submissions.

**Conflicts of Interest:** The authors declare no conflict of interest.

#### References

1. Gasko, K.L.; Janowski, G.M.; Pletka, B.J. The Influence of  $\gamma$ - $\gamma'$  Eutectic on the Mechanical Properties of Conventionally Cast MAR-M247. *Mater. Sci. Eng. A* **1988**, *104*, 1–8. [[CrossRef](#)]
2. Kim, I.S.; Choi, B.G.; Seo, S.M.; Kim, D.H.; Jo, C.Y. Influence of Heat Treatment on Microstructure and Tensile Properties of Conventionally Cast and Directionally Solidified Superalloy CM247LC. *Mater. Lett.* **2008**, *62*, 1110–1113. [[CrossRef](#)]
3. Baldan, R.; Silva, A.A.A.P.; Nunes, C.A.; Couto, A.A.; Gabriel, S.B.; Alkmin, L.B. Solution and Aging of MAR-M246 Nickel-Based Superalloy. *J. Mater. Eng. Perform.* **2017**, *26*, 465–471. [[CrossRef](#)]
4. Sajjadi, S.A.; Nategh, S.; Guthrie, R.I.L. Study of Microstructure and Mechanical Properties of High Performance Ni-base Superalloy GTD-111. *Mater. Sci. Eng. A* **2002**, *325*, 484–489. [[CrossRef](#)]
5. Kotval, P.S.; Venables, J.D.; Calder, R.W. The Role of Hafnium in Modifying the Microstructure of Cast Nickel-Base Superalloys. *Metall. Trans.* **1972**, *3*, 453–458. [[CrossRef](#)]
6. Henderson, M.B.; Arrell, D.; Larsson, R.; Heobel, M.; Marchant, G. Nickel Based Superalloy Welding Practices for Industrial Gas Turbine Applications. *Sci. Technol. Weld. Join.* **2004**, *9*, 13–21. [[CrossRef](#)]
7. Zhong, M.L.; Sun, H.Q.; Lin, W.J.; Zhu, X.F.; He, J.J. Boundary Liquation and Interface Cracking Characterization in Laser Deposition of Inconel 738 on Directionally Solidified Ni-Based Superalloy. *Scr. Mater.* **2005**, *53*, 159–164. [[CrossRef](#)]
8. Sidhu, R.K.; Ojo, O.A.; Chaturvedi, M.C. Microstructural Analysis of Laser-Beam-Welded Directionally Solidified INCONEL 738. *Metall. Mater. Trans. A* **2007**, *38*, 858–870. [[CrossRef](#)]
9. Montazeri, M.; Malek Ghaini, F.; Ojo, O.A. Heat Input and the Liquation Cracking of Laser Welded IN738LC Superalloy. *Weld. J.* **2013**, *92*, 258–264.

10. Shahsavari, H.A.; Kokabi, A.H.; Nategh, S. Effect of Preweld Microstructure on HAZ Liquation Cracking of Rene 80 Superalloy. *Mater. Sci. Technol.* **2007**, *23*, 547–555. [[CrossRef](#)]
11. Sidhu, R.K.; Ojo, O.A.; Chaturvedi, M.C. Microstructural Response of Directionally Solidified Rene 80 Superalloy to Gas-Tungsten Arc Welding. *Metall. Mater. Trans. A* **2009**, *40*, 150–162. [[CrossRef](#)]
12. Österle, W.; Krause, S.; Moelders, T.; Niedel, A.; Oder, G.; Völker, J. Influence of Heat Treatment on Microstructure and Hot Crack Susceptibility of Laser-Drilled Turbine Blades Made from Rene 80. *Mater. Charact.* **2008**, *59*, 1564–1571. [[CrossRef](#)]
13. Rush, M.T.; Colegrove, P.A.; Zhang, Z.; Broad, D. Liquation and Post-Weld Heat Treatment Cracking in Rene 80 Laser Repair Welds. *J. Mater. Process. Technol.* **2012**, *212*, 188–197. [[CrossRef](#)]
14. González, M.A.; Martínez, D.I.; Pérez, A.; Guajardo, H.; Garza, A. Microstructural Response to Heat Affected Zone Cracking of Prewelding Heat-Treated Inconel 939 Superalloy. *Mater. Charact.* **2011**, *62*, 1116–1123. [[CrossRef](#)]
15. González Albarrán, M.A.; Martínez, D.I.; Díaz, E.; Guzman, I.; Saucedo, E.; Guzman, A.M. Effect of Preweld Heat Treatment on the Microstructure of Heat-Affected Zone (HAZ) and Weldability of Inconel 939 Superalloy. *J. Mater. Eng. Perform.* **2014**, *23*, 1125–1130. [[CrossRef](#)]
16. Attallah, M.M.; Terasaki, H.; Moat, R.J.; Bray, S.E.; Komizo, Y.; Preuss, M. In-Situ Observation of Primary  $\gamma'$  Melting in Ni-Base Superalloy Using Confocal Laser Scanning Microscopy. *Mater. Charact.* **2011**, *62*, 760–767. [[CrossRef](#)]
17. Lachowicz, M.; Dudziński, W.; Hainmann, K.; Podrez-Radziszewska, M. Microstructure Transformations and Cracking in the Matrix of  $\gamma$ - $\gamma'$  Superalloy Inconel 713C Melted with Electron Beam. *Mater. Sci. Eng. A* **2008**, *479*, 269–276. [[CrossRef](#)]
18. Li, Q.; Lin, X.; Wang, X.H.; Yang, H.; Song, M.; Huang, W.D. Research on the Grain Boundary Liquation Mechanism in Heat Affected Zones of Laser Forming Repaired K465 Nickel-Based Superalloy. *Metals*. **2016**, *6*, 64. [[CrossRef](#)]
19. Ojo, O.A.; Richards, N.L.; Chaturvedi, M.C. On Incipient Melting During High Temperature Heat Treatment of Cast Inconel 738 Superalloy. *J. Mater. Sci.* **2004**, *39*, 7401–7404. [[CrossRef](#)]
20. Ojo, O.A.; Richards, N.L.; Chaturvedi, M.C. Study of the Fusion Zone and Heat-Affected Zone Microstructures in Tungsten Inert Gas-Welded Inconel 738LC Superalloy. *Metall. Mater. Trans. A* **2006**, *37*, 421–433. [[CrossRef](#)]
21. Ojo, O.A. Intergranular Liquation Cracking in Heat Affected Zone of a Welded Nickel Based Superalloy in As Cast Condition. *Mater. Sci. Technol.* **2007**, *23*, 1149–1155. [[CrossRef](#)]
22. Egbewande, A.T.; Zhang, H.R.; Sidhu, R.K.; Ojo, O.A. Improvement in Laser Weldability of Inconel 738 Superalloy through Microstructural Modification. *Metall. Mater. Trans. A* **2009**, *40*, 2694–2704. [[CrossRef](#)]
23. Egbewande, A.T.; Buckson, R.A.; Ojo, O.A. Analysis of Laser Beam Weldability of Inconel 738 Superalloy. *Mater. Charact.* **2010**, *61*, 569–574. [[CrossRef](#)]
24. Montazeri, M.; Ghaini, F.M. The Liquation Cracking Behavior of IN738LC Superalloy during Low Power Nd:YAG Pulsed Laser Welding. *Mater. Charact.* **2012**, *67*, 65–73. [[CrossRef](#)]
25. Banerjee, K.; Richards, N.L.; Chaturvedi, M.C. Effect of Filler Alloys on Heat-Affected Zone Cracking in Preweld Heat-Treated IN-738 LC Gas-Tungsten-Arc Welds. *Metall. Mater. Trans. A* **2005**, *36*, 1881–1890. [[CrossRef](#)]

